



**HAL**  
open science

## Phase transformation in SiO<sub>x</sub>/SiO<sub>2</sub> multilayers for optoelectronics and microelectronics applications

Manuel Roussel, Etienne Talbot, R.P. Nalini, Fabrice Gourbilleau, Philippe Pareige

### ► To cite this version:

Manuel Roussel, Etienne Talbot, R.P. Nalini, Fabrice Gourbilleau, Philippe Pareige. Phase transformation in SiO<sub>x</sub>/SiO<sub>2</sub> multilayers for optoelectronics and microelectronics applications. *Ultramicroscopy*, 2013, 132, pp.290. 10.1016/j.ultramic.2012.10.013 . hal-00861764

**HAL Id: hal-00861764**

**<https://hal.science/hal-00861764>**

Submitted on 26 Jun 2018

**HAL** is a multi-disciplinary open access archive for the deposit and dissemination of scientific research documents, whether they are published or not. The documents may come from teaching and research institutions in France or abroad, or from public or private research centers.

L'archive ouverte pluridisciplinaire **HAL**, est destinée au dépôt et à la diffusion de documents scientifiques de niveau recherche, publiés ou non, émanant des établissements d'enseignement et de recherche français ou étrangers, des laboratoires publics ou privés.

# Phase transformation in SiO<sub>x</sub>/SiO<sub>2</sub> multilayers for optoelectronics and microelectronics applications

M. Roussel<sup>a</sup>, E. Talbot<sup>a,\*</sup>, R. Pratibha Nalini<sup>b</sup>, F. Gourbilleau<sup>b</sup>, P. Pareige<sup>a</sup>

<sup>a</sup> Groupe de Physique des Matériaux, Université et INSA de Rouen, UMR CNRS 6634, Avenue de l'Université, BP 12, 76801 Saint Etienne du Rouvray, France, Europe

<sup>b</sup> Centre de Recherche sur les Ions, les Matériaux et la Photonique (CIMAP), CEA/CNRS/ENSICAEN/UCBN, 6 Bd. Maréchal Juin, 14050 Caen Cedex 4, France, Europe

## A B S T R A C T

Due to the quantum confinement, silicon nanoclusters (Si-ncs) embedded in a dielectric matrix are of prime interest for new optoelectronics and microelectronics applications. In this context, SiO<sub>x</sub>/SiO<sub>2</sub> multilayers have been prepared by magnetron sputtering and subsequently annealed to induce phase separation and Si clusters growth. The aim of this paper is to study phase separation processes and formation of nanoclusters in SiO<sub>x</sub>/SiO<sub>2</sub> multilayers by atom probe tomography. Influences of the silicon supersaturation, annealing temperature and SiO<sub>x</sub> and SiO<sub>2</sub> layer thicknesses on the final microstructure have been investigated. It is shown that supersaturation directly determines phase separation regime between nucleation/classical growth and spinodal decomposition. Annealing temperature controls size of the particles and interface with the surrounding matrix. Layer thicknesses directly control Si-nc shapes from spherical to spinodal-like structures.

## Keywords:

Silicon nanocluster, Multilayers  
Phase transformation, Optoelectronics  
Atom probe Tomography.

## 1. Introduction

In 1990 Canham [1] discovered that porous silicon exhibits photoluminescence properties. Since this discovery, Si nanostructures have been thoroughly studied for their optical and electrical properties. Among these structures, Si-ncs embedded in a dielectric matrix have attracted much interest. A 4 nm diameter Si-nc or smaller permits transformation of Si band gap from indirect to direct, offering new optical properties to silicon. Si-ncs also exhibit interesting electrical properties as a trap for electrons. These new properties for Si can be used for new generation of solar cells [2], waveguide amplifiers [3] or non volatile-memories [4]. Besides, using Si-ncs in SiO<sub>2</sub> is fully compatible with the existing Si-based CMOS (Complementary metal-oxide-semiconductor) technology.

Optical and electrical properties of Si-ncs are highly dependent on the structure of Si-ncs and their surroundings. For instance, the particles size directly determines the band gap of these systems [5]. As for the composition of the surrounding oxide and the particles interface, it influences light emission and charge storage [6,7]. Thus, it is crucial to control these structural parameters during the fabrication of Si-ncs. Synthesis of Si-ncs usually consists in enriching silica with Si by deposition processes [2] or implantation [8]. The silicon-rich silica (SiO<sub>x</sub>) is then annealed in

order to induce phase separation between Si and SiO<sub>2</sub> as predicted by the Si–O phase diagram [9]. A simple way to achieve size control of the Si-ncs is to sandwich silicon-rich thin layers between two silica layers in a multilayered structure. During the annealing process, silica acts as a diffusion barrier and limits the Si-ncs growth [2,10]. In order to control the nanostructure of Si-nc based materials, it is of prime interest to understand the phase separation process and the Si-nc growth mechanisms.

Atomic analysis tools are crucial to perform such a study. Numerous techniques have been employed in order to study the correlation between structural characteristics (SIMS [11], XRD [12]) and optical or electrical properties (photoluminescence measurements [2,5,8,10], C–V curves [5], and charge spectroscopy [13]). To date electron microscopy is generally used in order to characterize Si-nc based materials. For instance, HRTEM allows the detection of crystallized Si-ncs in amorphous silica if they are oriented in diffraction conditions [14]. Recent studies report that Energy Filtered TEM is able to image amorphous clusters, allowing for a more accurate size distribution measurement than HRTEM [15]. Yet, as mentioned by Schamm et al., Si phase identification depends on the deconvolution of Si peak on Electron energy loss spectroscopy (EELS) spectra and on contrast enhancement. Typically, this can lead to small changes in the size distribution of Si-nc depending on the data treatment which is applied to the TEM images. Besides it gives access to only planar projections which leads to superposition of several particles in the case of a multilayered structure. Oxide composition also can be extrapolated from EELS spectra but only under drastic assumptions such as

\* Corresponding author. Tel.: +33 2 32 95 51 32; fax: +33 2 32 95 50 32.  
E-mail address: etienne.talbot@univ-rouen.fr (E. Talbot).

monodispersed Si-ncs [16]. Characterizing the structural properties of silicon nanoparticles based materials has become a major challenge and investigating Si-ncs growth process has become crucial for the development of new optical devices.

In this paper, we propose to use the three dimensional chemical map provided by atom probe tomography in order to study the phase separation processes into  $\text{SiO}_x$ . It has been demonstrated that atom probe is able to provide an accurate description of these systems and gives accurate information about size distribution, number density of particles and matrix composition [17]. Several  $\text{SiO}_x/\text{SiO}_2$  multilayers (MLs) have been synthesized in order to study the influences of three parameters on the decomposition: (i) the initial supersaturation, (ii) the annealing treatment and (iii) the thickness of  $\text{SiO}_x$  and  $\text{SiO}_2$  layers.

## 2. Experimental

The MLs have been synthesized by reactive magnetron sputtering. Pure  $\text{SiO}_2$  targets have been sputtered on [100] oriented 2" silicon wafers with a power density of  $1.3 \text{ Wcm}^{-2}$  at  $650^\circ\text{C}$ . Pure Ar plasma is used to deposit  $\text{SiO}_2$  layers and 50%  $\text{H}_2 + 50\%$  Ar plasma is used to deposit  $\text{SiO}_x$  layers. As hydrogen reduces oxygen, the deposited oxide is not stoichiometric and contains approximately 50% of silicon. This composition corresponds to 25% of silicon excess of silicon in  $\text{SiO}_2$  in the  $\text{A}^{900}$  multilayer. The addition of silicon chips onto the silica target permits reaching higher silicon content and tuning the composition of the film ( $\text{B}^{\text{xx}}$ ,  $\text{C}^{\text{xx}}$  and  $\text{D}^{\text{xx}}$  samples). The sputtering time controls the thickness of  $\text{SiO}_x$  and  $\text{SiO}_2$  layers. This process was fully described in a previous paper [10]. After deposition, samples are annealed for 1 h at different temperatures under a  $\text{N}_2$  atmosphere. The samples prepared with different supersaturation, different thicknesses and different annealing temperatures are summarized in Table 1.

Structural analysis has been carried out using both HRTEM and atom probe tomography. HRTEM images have been obtained on a Topcon 002B. The cross section view of the sample and the identification of crystalline Si-ncs permit confirming the thickness of the deposited layers. This thickness measurement is realized on each synthesized sample (Fig. 1a).

A full description of the atom probe tomography principle and the sample preparation can be found in the literature [18–21]. Sample preparation consists of tip-shaping of specimen using a dual beam Zeiss NVision 40 FIB-SEM. To do so, multilayers are extracted from the wafer using a lift-out method, mounted on a stainless steel needle, and sharpened by annular milling. Specimen preparation has been described in detail by Thompson et al. [22]. At the end of this process, the specimen must have a curvature radius below 50 nm. This tip is placed under high vacuum ( $\approx 10^{-8}$  Pa), at low temperature (80 K) and high positive voltage is applied on the tip ( $\approx 5\text{--}15$  kV). The superposition of UV laser pulses (343 nm, 50 nJ, 350 fs, 100 kHz) triggers ionization of the specimen surface atoms which are accelerated toward a

**Table 1**

List of sample characteristics for each elaborated multilayer.

| Sample            | Annealing temperature ( $^\circ\text{C}$ ) | silicon Excess (%) | $\text{SiO}_x$ thickness (nm) | $\text{SiO}_2$ thickness (nm) |
|-------------------|--|--------------------|-------------------------------|-------------------------------|
| $\text{A}^{900}$  | 900  | 25                 | 4                             | 4                             |
| $\text{B}^{900}$  | 900  | 30                 | 4                             | 3                             |
| $\text{B}^{1000}$ | 1000                                       | 30                 | 4                             | 3                             |
| $\text{B}^{1100}$ | 1100                                       | 30                 | 4                             | 3                             |
| $\text{C}^{900}$  | 900  | 30                 | 8                             | 10                            |
| $\text{C}^{1100}$ | 1100                                       | 30                 | 8                             | 10                            |
| $\text{D}^{900}$  | 900  | 30                 | 4                             | 1.5                           |
| $\text{D}^{1100}$ | 1100                                       | 30                 | 4                             | 1.5                           |

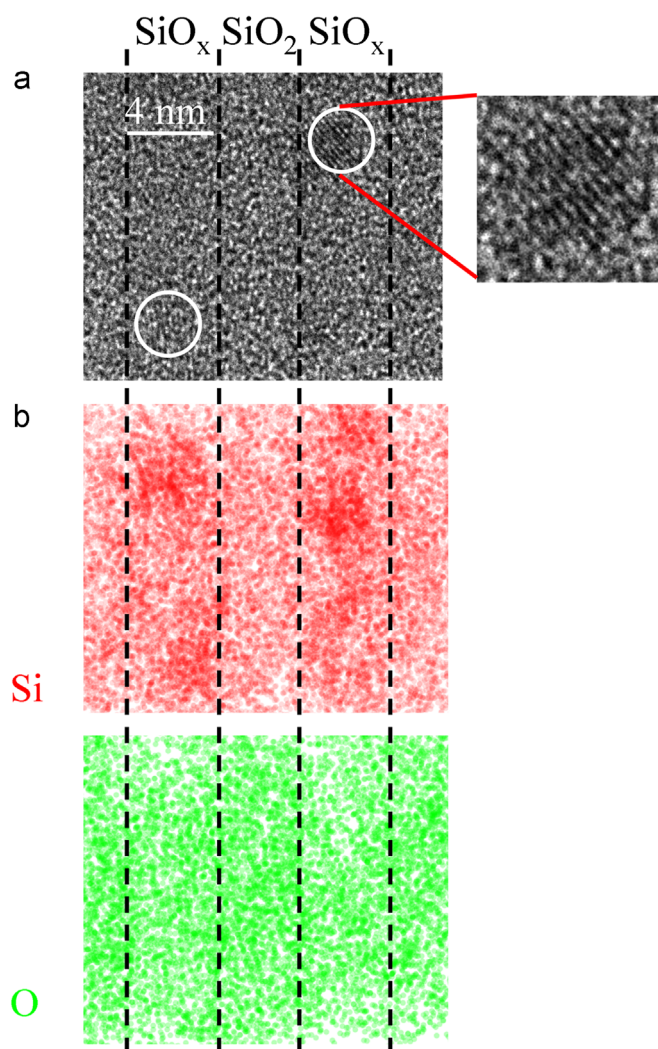


**Fig. 1.** (a) HRTEM cross sectional image of  $\text{A}^{900}$  multilayer. White circles evidence crystalline structures, (b) Silicon and oxygen maps obtained in LAWATAP on the same multilayer. Dash lines evidence Si-rich and  $\text{SiO}_2$  layers.

position sensitive detector. Their chemical natures are identified by time of flight mass spectrometry. The position ( $X$  and  $Y$ ) of an ion when it leaves the tip is deduced from the position of its impact on the detector. The magnification, the atomic volume of each evaporated ion, and the efficiency of the detector permit the calculation of the third dimension ( $Z$ ). In our case the efficiency of the detector is  $Q=60\%$ . During the 3D reconstruction, the thickness of each  $\text{SiO}_2/\text{SiO}_x$  bilayer is kept constant and is deduced from HRTEM calibration as illustrated in Fig. 1b. The same layered system has been imaged using HRTEM and analyzed using a Laser Assisted Wide Angle Tomographic Atom Probe. Identification of the Si-rich layers in HRTEM is based on the identification of crystalline clusters. The Si-rich layers are clearly evidenced by higher silicon density on atom probe reconstructions. This reconstruction method, combining electron microscopy and atom probe tomography, permits avoiding artefacts related to the different compositions of  $\text{SiO}_x$  and  $\text{SiO}_2$  layers as observed in the work of Thompson et al. [23].

Evaporation of different phases during atom probe experiments leads to local magnification effects. This artefact is well known and well documented in the atom probe tomography community. In the case of silicon clusters embedded in a  $\text{SiO}_2$  matrix, Si-ncs have the lowest evaporation field. Si atoms belonging to Si-ncs evaporate faster than atoms of  $\text{SiO}_2$  matrix, inducing local variations of curvature radius and changes in ions

trajectories. Due to these aberrations, a pure spherical Si-nc will appear compressed along  $X$  and  $Y$  directions and diluted after 3D reconstruction. This artefact is taken into account during data treatment, following the process proposed by Blavette et al. [24] and Vurpillot et al. [25] which permits calculating the influence of trajectory aberrations on the composition of a precipitate. This method has already been applied on similar materials by Talbot et al. [14]. In this paper, authors have demonstrated that the evaporation of pure spherical Si-ncs surrounded by stoichiometric  $\text{SiO}_2$  shells can lead to 3D reconstructions showing Si-ncs containing up to 20 at% of oxygen coming from the surrounding silica matrix. Combined with HRTEM results, the authors have proposed a correction to evidence the pure Si core of the Si-ncs. Consequently, all Si-rich regions containing more than 80 at% of silicon will be considered as pure silicon. However, the presented volumes are raw 3D reconstructions where the local magnification effect and the trajectory aberrations have not been corrected.

### 3. Results and discussion

#### 3.1. Influence of supersaturation

We have investigated the decomposition process in samples  $A^{900}$  and  $B^{900}$ . As reported in Table 1, both of these samples contain 4 nm – thick  $\text{SiO}_x$  layers which have been annealed for 1 h at 900 °C. However, according to the synthesis conditions,  $\text{SiO}_x$  layers contain more silicon excess in  $B^{900}$  than  $A^{900}$ . After atom probe analysis, composition measurements are carried out in Si-rich layers in both samples. As predicted during the synthesis process, supersaturation is higher in  $B^{900}$  Si-rich layers than in  $A^{900}$ . In  $A^{900}$ ,  $\text{SiO}_x$  layers contain  $51.0 \pm 0.3$  at% of silicon (corresponding to 26% of silicon excess in  $\text{SiO}_2$ ). In  $B^{900}$ , the silicon content in Si-rich layer is  $53.7 \pm 0.1$  at%

(corresponding to 31% of silicon excess in  $\text{SiO}_2$ ). Fig. 2a and b present 60%-silicon isoconcentration surfaces (red polygons) in both samples. In  $A^{900}$ , Si-rich areas are isolated from each other and appear to be spherical. In  $B^{900}$ , Si-rich areas are interconnected and show noodle shapes. In order to characterize the interface of Si-rich regions, 2-dimensionnal concentration maps have been added to these isoconcentration surfaces. On these maps, zones which contain more than 80% of silicon appear in red. Aforementioned, these zones correspond to pure silicon. Zones which contain less than 33% of silicon appear in black. In  $A^{900}$  sample, Si-ncs appear as highly concentrated areas separated from each other by silicon oxide (close to silica composition). In the case of  $B^{900}$  sample, Si-rich areas appear as diffuse interconnected composition fluctuations.

Thus, a change of silicon excess in the  $\text{SiO}_x$  film drastically changes the structure of the film after annealing. For the lowest supersaturation we observe spherical Si-ncs with abrupt interfaces which are the signature of nucleation and classical growth. Increasing supersaturation leads to a different phase separation process: spinodal decomposition [26]. This implies that the spinodal limit in the Si–O phase diagram should be between 50 and 54 at% of silicon at 900 °C. This limit for spinodal decomposition is not predicted in existing phase diagrams [9]. Moreover, it is not possible to calculate the spinodal limit assuming a classical regular solid solution model [27] since it is not possible to obtain free enthalpy curves for this system because  $\text{SiO}_2$  is a stoichiometric compound and pure oxygen is gaseous at this temperature.

#### 3.2. Influence of annealing temperature

In order to study the influence of the annealing treatment on the microstructure, sample B has been annealed for three different temperature: 900 °C ( $B^{900}$ ), 1000 °C ( $B^{1000}$ ) and 1100 °C ( $B^{1100}$ ).

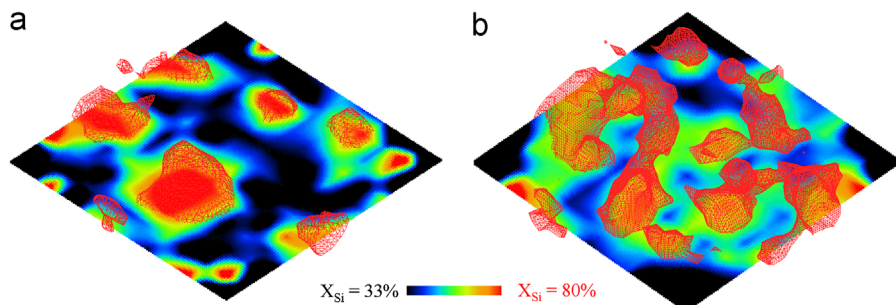


**Fig. 2.** A single  $\text{SiO}_x$  layer in a) sample  $A^{900}$  and b) sample  $B^{900}$ . 60%-silicon isoconcentration surfaces are represented by red polygons. Two-dimensional concentration maps range from 33% of silicon (black) to 80% of silicon (red)(volume:  $12 \times 12 \times 6 \text{ nm}^3$ ). (For interpretation of the references to color in this figure legend, the reader is referred to the web version of this article.)

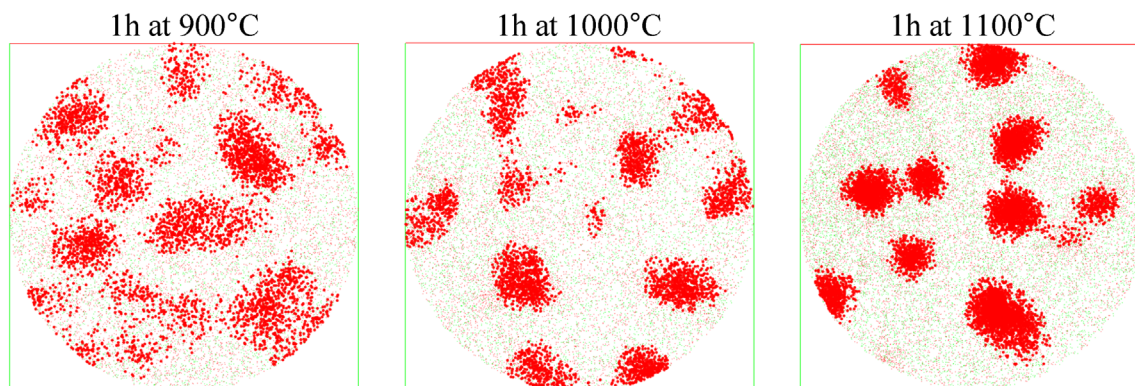


**Fig. 3.** Plan view of a single  $\text{SiO}_x$  layer in samples  $B^{900}$ ,  $B^{1000}$  and  $B^{1100}$ . Bold dots represent silicon atoms belonging to Si-rich areas containing more than 55% of silicon (volume:  $12 \times 12 \times 6 \text{ nm}^3$ ).

In Fig. 3, a cluster identification data treatment evidences Si-rich areas ( $\geq 55$  at%) in  $\text{SiO}_x$  layers. Aforementioned,  $B^{900}$  shows interconnected diffuse concentration fluctuations which are characteristics of spinodal decomposition. Increasing the annealing temperature in  $B^{1000}$  and  $B^{1100}$  leads to the replacement of interconnected Si-rich regions by isolated Si-ncs.

Increasing the temperature leads to a completely different microstructure. The composition fluctuations that we observed in  $B^{900}$  are replaced by a two-phase system containing Si-ncs as shown in  $B^{1000}$  and  $B^{1100}$ . This microstructure corresponds to late stage of spinodal decomposition during coarsening of Si-rich regions. This is in good agreement with low silicon content measured in  $B^{1000}$  and  $B^{1100}$  matrix: respectively  $35.8 \pm 0.6$  at% and  $32.7 \pm 0.3$  at% of silicon.

Usually late stages of spinodal decomposition exhibit noodle-like concentrated areas with sharp interfaces which are coarsening. This type of interconnected structure is not observed in  $B^{1000}$  and  $B^{1100}$ . This different structure has two potential explanations: i) It is possible that these temperatures are above the spinodal limit in the phase diagram but, as mentioned previously, it is not possible to define clearly this limit. However, given the extremely low solubility limit of Si in  $\text{SiO}_2$  [9], the spinodal limit should not vary from 900 °C to 1100 °C. ii) Another explanation is given by Seol et al. who studied spinodal decomposition in thin films by mean of phase field simulations [28]. Their work shows that when the thickness of the film is smaller than the wavelength of composition fluctuations, spinodal decomposition leads to the development of self-arranged columnar composition fluctuations. Therefore, late stage of decomposition leads to the development of isolated clusters instead of interconnected structures, as observed in  $B^{1000}$  and  $B^{1100}$ . In order to investigate the influence of the thickness of the film, samples with different  $\text{SiO}_x$  and  $\text{SiO}_2$  thicknesses are discussed in the following.

### 3.3. Influence of layer thicknesses

In order to investigate the influence of  $\text{SiO}_x$  and  $\text{SiO}_2$  thicknesses, samples with different  $\text{SiO}_x$  and  $\text{SiO}_2$  sublayer thicknesses have been analyzed (samples  $B^{xx}$ ,  $C^{xx}$  and  $D^{xx}$ ). Each one of this sample has been annealed at 900 °C and 1100 °C and their 3D reconstruction are presented in Fig. 4. In these 3D reconstructions, surfaces of isoconcentration (at 55% of silicon) are represented by red polygons. At 900 °C, all  $\text{SiO}_x$  layers exhibit interconnected structures attributed to spinodal decomposition. After 1h at 1100 °C,  $B^{1100}$ ,  $C^{1100}$  and  $D^{1100}$  exhibit pure Si-rich areas with abrupt interfaces while the matrix is pure silica in all three samples. However we observe three completely different structures.

The  $B^{1100}$  sample which is composed of 4 nm  $\text{SiO}_x$  layers and 3 nm  $\text{SiO}_2$  layers where Si-ncs are arranged in  $\text{SiO}_x$  layers was described in the previous sections. In this case the multilayered structure is still observed and the mean diameter of the particles is  $3.2 \pm 0.1$  nm.

The  $C^{1100}$  sample is composed of 8 nm  $\text{SiO}_x$  layers and 10 nm  $\text{SiO}_2$  layers which are still arranged in multilayer disposition. In this case, the Si-rich areas are not spherical. These silicon rich structures correspond to the late stage of spinodal decomposition. This observation is an experimental evidence of Seol et al. predictions about the influence of the thickness of the film on the spinodal decomposition process [28]. It appears that decreasing the thickness of the Si-rich film induces the disappearance of typical spinodal interconnected structure to self-arranged Si-ncs.

In D samples,  $\text{SiO}_x$  thickness is kept to 4 nm. However thickness of the  $\text{SiO}_2$  barrier has been decreased to 1.5 nm. One hour annealing at 1100 °C induces the formation of Si-rich structures. Some of these structures appear to be spherical Si-nc whereas

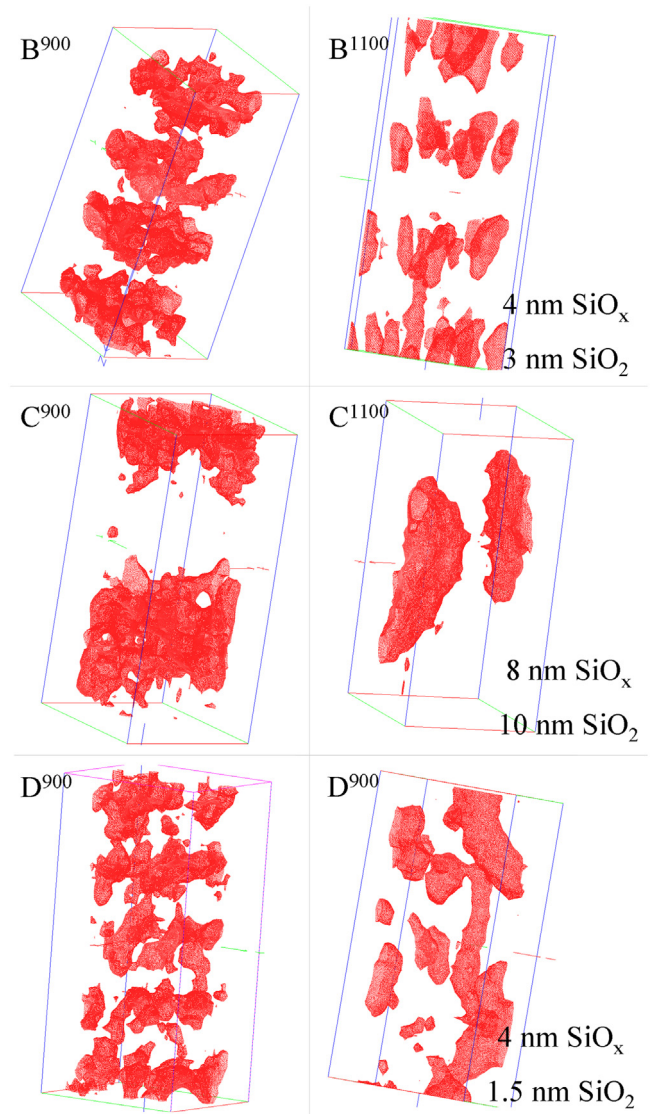


**Fig. 4.** Silicon-rich areas in samples  $B^{900}$ ,  $B^{1100}$ ,  $C^{900}$ ,  $C^{1100}$ ,  $D^{900}$  and  $D^{1100}$ . Surfaces of isoconcentration (55 at% of silicon) are represented by red polygons. (volume:  $12 \times 12 \times 25 \text{ nm}^3$ ). (For interpretation of the references to color in this figure legend, the reader is referred to the web version of this article.)

others are composed of several coalescing Si-ncs, forming more complex shapes (such as tubes and ellipsoids). In this case no layered structure can be observed and this loss of the layered structure is related to the mean free path of a silicon atom into  $\text{SiO}_2$ . The diffusion coefficient of silicon in silica given by Tsoukalas et al. [29] at 1100 °C is  $D=5.7 \times 10^{-18} \text{ cm}^2 \text{ s}^{-1}$ . The mean free path of a Si atom in  $\text{SiO}_2$  at this temperature, for  $t=3600 \text{ s}$ , is roughly given by  $d=\sqrt{Dt} \approx 1.5 \text{ nm}$ . Hence, it is possible for silicon to diffuse through the silica barrier, and the  $\text{SiO}_x/\text{SiO}_2$  stacking sequence is no longer visible after annealing.

## 4. Conclusions

The need for analysis tool able to image accurately Si-nc based systems is a major challenge for optoelectronics and microelectronics. In this paper, we have demonstrated that atom probe tomography is able to provide new information about these systems. The influences of annealing temperature, silicon supersaturation and layer thicknesses on phase separation processes in  $\text{SiO}_x/\text{SiO}_2$

multilayers have been investigated. We demonstrated that the annealing treatment controls kinetics of the phase transformation and determines the composition of the oxide surrounding Si-ncs. As for the influence of the supersaturation, SiO<sub>x</sub> films containing 51 at% of silicon have been annealed which lead to Si-nc nucleation and growth while 54 at% of silicon in the SiO<sub>x</sub> film leads to spinodal decomposition. In the case of 8 nm layers (sample C<sup>1100</sup>), spinodal decomposition induces the formation of non-spherical interconnected Si-nc. This sample contains Si-rich objects larger than 5 nm, which is the size limit for quantum confinement effects. In 4 nm SiO<sub>x</sub> films, spinodal decomposition leads to the formation of arrays of isolated Si-ncs ranging from 1 nm to 4 nm which are fully compatible with quantum confinement requirements.

SiO<sub>2</sub> diffusion barriers also play an important role during the phase separation process. As evidenced by sample B<sup>1100</sup>, 3 nm thick SiO<sub>2</sub> barriers are efficient and limit silicon diffusion in two dimensions during 1 h annealing at 1100 °C. However, for the same annealing treatment, we observed that 1.5 nm barriers are not sufficient. In this case the layered structure is lost after annealing.

### Acknowledgments

This work was supported by the upper Normandy Research and the French Ministry of Research in the framework of Research Networks of Upper-Normandy. The authors acknowledge also "Le Fond Européen de Développement Régional (FEDER) for support.

### References

- [1] L. Canham, *Applied Physics Letters* 57 (1990) 1046.
- [2] F. Gourbilleau, C. Ternon, D. Maestre, O. Palais, C. Dufour, *Journal of Applied Physics* 106 (2009) 013501.
- [3] M. Fujii, M. Yoshida, Y. Kanzawa, S. Hayashi, K. Yamamoto, *Applied Physics Letters* 71 (1997) 1198.
- [4] S. Tiwari, F. Rana, H. Hanafi, A. Harstein, E. Crabbe, K. Chan, *Applied Physics Letters* 68 (1996) 1377.
- [5] T. Creazzo, B. Redding, E. Marchena, J. Murakowski, D. Prather, *Journal of Luminescence* 130 (2010) 631.
- [6] O. Jambois, H. Rinnert, X. Devaux, M. Vergnat, *Journal of Applied Physics* 98 (2005) 046105.
- [7] A. Romanyuk, V. Melnik, Y. Olikh, J. Biskupek, U. Kaiser, M. Feneberg, K. Thonke, P. Oelhafen, *Journal of Luminescence* 130 (2010) 87.
- [8] S. Guha, M. Pace, D. Dunn, I. Singer, *Applied Physics Letters* 70 (1997) 1207.
- [9] S.M. Schnurre, J. Gröbner, R. Schmid-Fetzer, *Journal of Non-Crystalline Solids* 336 (2004) 1.
- [10] C. Ternon, F. Gourbilleau, X. Portier, P. Voidevel, C. Dufour, *Thin Solid Films* 419 (2002) 5.
- [11] M. Perego, S. Ferrari, M. Fanciulli, G. Ben Assayag, C. Bonafos, M. Carrada, A. Claverie, *Applied Surface Science* 231–232 (2004) 813.
- [12] D. Comedi, O.H.Y. Zalloum, E.A. Irving, J. Wojcik, T. Roschuk, M.J. Flynn, P. Mascher, *Journal of Applied Physics* 99 (2006) 023518.
- [13] I. Antonova, E. Neustroev, S. Smagulova, J. Jedrzejewski, *Physica Status Solidi C* 6 (2009) 2704.
- [14] E. Talbot, R. Lardé, F. Gourbilleau, C. Dufour, P. Pareige, *Europhysics Letters* 87 (2009) 26004.
- [15] S. Schamm, C. Bonafos, H. Coffin, N. Cherkashin, M. Carrada, G. Ben Assayag, A. Claverie, M. Tencé, C. Colliex, *Ultramicroscopy* 108-4 (2008) 346.
- [16] C. Spinella, C. Bongiorno, G. Nicotra, E. Rimini, A. Muscara, S. Coffa, *Applied Physics Letters* 87 (2009) 044102.
- [17] M. Roussel, E. Talbot, F. Gourbilleau, P. Pareige, *Nanoscale Research Letters* 6 (2011) 164.
- [18] T.F. Kelly, M.K. Miller, *Review of Scientific Instruments* 78 (2007) 031101.
- [19] M.K. Miller, A. Cerezo, M.G. Hetherington, G.D.W. Smith, *Atom Probe Field Ion Microscopy*. Oxford 24 (27) (1996) 33 3, 6.
- [20] T. Tsong, *Atom-Probe Field Ion Microscopy: Field Ion Emission and Surfaces and Interfaces at Atomic Resolution*, 3, Cambridge University Press, 1990 20.
- [21] E.W. Müller, T.T. Tsong, *Field Ion Microscopy* 3 (5) (1969) 7.
- [22] K. Thompson, D. Lawrence, D.J. Larson, J.D. Olson, T.F. Kelly, B. Gorman, *Ultramicroscopy* 107 (2007) 131.
- [23] G.B. Thompson, M.K. Miller, H.L. Fraser, *Ultramicroscopy* 100 (2004) 25.
- [24] F. Vurpillot, A. Bostel, D. Blavette, *Applied Physics Letters* 76 (2000) 3127.
- [25] D. Blavette, F. Vurpillot, P. Pareige, A. Menand, *Ultramicroscopy* 89 (2001) 145.
- [26] J.W. Cahn, *Acta Metallurgica* 9 (1961) 795.
- [27] D.A. Porter, K.E. Easterling, M.Y. Sherif, third edition, *Phase Transformations in Metals and Alloys*, 13, CRC press, 2009.
- [28] D.J. Seol, S.Y. Hu, Y.L. Li, J. Shen, K.H. Oh, L.Q. Chen, *Acta Materialia* 51 (2003) 5173.
- [29] D. Tsoukalas, C. Tsamis, P. Normand, *Mat. Res., Society Symposium Proceedings* 669 (J3) (2001) 7.1.